Journal of Solid State Chemistry **156,** 379–389 (2001)
doi:10.1006/jssc.2000.9009, available online at http://www.idealibrary.com on IDEAL®

Structural Disorder and Ionic Conductivity in $LiVO_3$: A Neutron Powder Diffraction Study from 340 to 890 K

Ch. Muller,* J.-C. Valmalette,* J.-L. Soubeyroux,† F. Bouree,‡ and J.-R. Gavarri*

*Laboratoire L2MP/MMI – CNRS, Université de Toulon et du Var, BP 132, 83957 La Garde Cedex, France; †Laboratoire de Cristallographie – CNRS and Institut Laue-Langevin, BP 166, 38042 Grenoble Cedex 09, France; and ‡Laboratoire Léon Brillouin, CE-Saclay, 91191 Gif-sur-Yvette, France

Received July 25, 2000; in revised form October 5, 2000; accepted October 13, 2000; published online December 21, 2000

The structure of the lithium metavanadate $LiVO_3$ has been refined at room temperature from high-resolution neutron powder diffraction data. The unit cell dimensions are $a = 10.1597_{(4)}$, $b = 8.4155_{(3)}$, $c = 5.8843_{(2)}$ Å, $\beta = 110.505^{\circ}_{(2)}$, and $V = 471.23_{(1)}$ Å^3 in the monoclinic space group $C2/c$ with $Z = 8$. Conventional R_p and R_{wp} reliability factors are respectively equal to 0.030 and 0.036. The structure consists of an alternating, along the *b*-axis, of bands of distorted LiO_6 octahedra running parallel to the *c*-axis which are linked by chains of VO_4 tetrahedra which are also parallel to the *c*-axis. The structural behavior of the ionic conductor $LiVO_3$ has been studied from neutron powder thermodiffractometry in the temperature range 340–890 K in order (i) to confirm the nature of the mobile species, (ii) to characterize the diffusion mechanisms, and (iii) to link the structural disorder existing in $LiVO_3$ to the high observed ionic conductivity.

Key Words: **pyroxene structure; neutron powder diffraction; ionic conductivity; structural disorder; Li^+ ion mobility; solid–liquid transition.**

1. INTRODUCTION

The Li–V–O system attracts a lot of interest for its applications in rechargeable lithium batteries or in solid oxide fuel cells. The lithium metavanadate $LiVO_3$ is among the potential candidates as solid electrolyte material or electrode material. Its crystal structure, first determined by Shannon and Calvo in 1973 by X-ray single crystal diffraction, has been described as a monoclinic pyroxene-type structure with space group $C2/c$ (clinopyroxene form) in which bands of LiO_6 octahedra are linked by chains of VO_4 tetrahedra parallel to the *c*-axis (1).

Electrical conductivity measurements, performed between room temperature and 820 K by impedance spectroscopy (Fig. 1), have shown a drastic change in the slope of the Arrhenius plot at approximately 690 K, the ionic conductivity rapidly increasing with the temperature above 690 K ($\sigma \approx 10^{-4}$ S cm^{-1} at 820 K) (2). The activation energy below 690 K is equal to 0.14 eV, which is the order of magnitude of the activation energies generally measured in the Li^+ cationic conductors.

In this paper, neutron powder diffraction data have been analyzed:

— at room temperature, in order to produce accurate nuclear density maps from a reinvestigation of the $LiVO_3$ structure and to correlate the anisotropic atomic displacements on the lithium sites to the high observed electrical conductivity;

— at high temperature (temperature range 340–890 K), in order to study, by means of thermodiffractometry, the thermal behavior of the structural parameters in relation to the enhanced electrical properties. Several structural parameters have been followed up to the solid-to-liquid transition.

The final aims of this work are to confirm the nature of the mobile species, to characterize the diffusion mechanisms, and to link the structural disorder existing in $LiVO_3$ to the high observed ionic conductivity.

2. EXPERIMENTAL

2.1. Sample Synthesis

The $LiVO_3$ powdered sample was prepared by direct solid-state reaction between Li_2CO_3 and V_2O_5. Starting powders from Aldrich (with purities of 99.997 and 99.99%, respectively) were initially dried and well ground in an agate mortar to give a uniform mixture, and then heated in air at 860 K for 12 h. Additional grinding was followed by thermal annealing for 24 h to ensure good homogeneity and to enhance the crystallization of the powder. The obtained powder was brown and deliquescent. The sample was placed under dried atmosphere for further experiments. An X-ray powder diffraction pattern, collected on Siemens–Bruker D5000 diffractometer (Cu$K\alpha$ radiation, back monochromator), was compared with the JCPDS data files: only the crystallized phase of $LiVO_3$ was identified and no impurity was detected.

0022-4596/01 $35.00

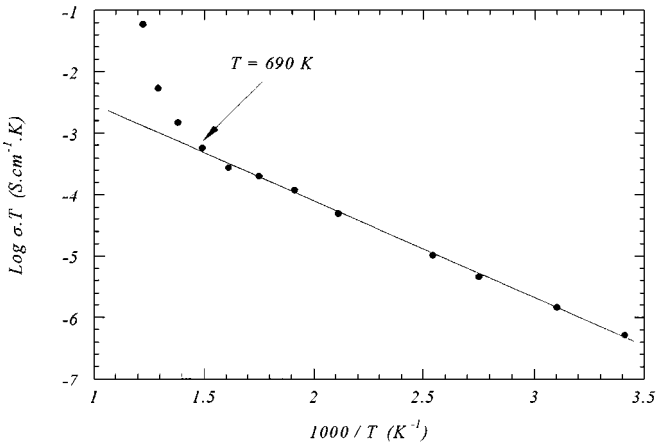

FIG. 1. Arrhenius plot of the electrical conductivity measured by impedance spectroscopy on a pellet of $LiVO_3$ in the temperature range 290–820 K.

2.2. Data Collection

A first neutron powder diffraction experiment was performed on the high-resolution diffractometer 3T2 at the Orphée reactor at the Laboratoire Léon Brillouin (CE-Saclay, France) with an incident wavelength of 1.2251 Å. The powdered $LiVO_3$ sample was sealed in a vanadium can and a diffraction pattern was recorded at room temperature. The 3T2 instrument is equipped with a bank of 20 ^{3}He detectors and the complete pattern acquisition is achieved by sweeping in steps of 0.05°. Full experimental details are summarized in Table 1.

A second set of neutron powder diffraction data was collected on the high-flux diffractometer D1B (Institut Laue-Langevin, Grenoble–France) equipped with a fixed position-sensitive detector (PSD) formed by a bank of 400 ^{3}He cells. The powder, in a vanadium can, was heated in a furnace under dynamic vacuum from 340 to 890 K. Diffraction patterns were recorded in the angular domain 27.0–106.8° (2θ) in steps of 0.2°, with an incident wavelength of 2.525 Å. Experimental details are given in Table 2.

2.3. Fitting Procedure

Full profile fitting refinements of the high-resolution neutron powder diffraction pattern were performed using the program *Fullprof* based on the Rietveld method (3). The observed diffraction peak profiles were described using a pseudo-Voigt profile shape function ($\eta \approx 0.3$). The angular dependence of the full width at half maximum (FWHM) of the diffraction peaks was chosen to be of Caglioti type ($\mathrm{FWHM}(\theta) = \sqrt{U \cdot \tan^2\theta + V \cdot \tan\theta + W}$, where U, V, and W are refinable parameters) (4). Systematic error corrections (zero-point shift and asymmetry) were applied. The background was adjusted from a polynomial function and a Debye function which takes the form $A(\sin Qd/Qd)$, where Q is the scattering vector, d is a pair correlation distance, and A the amplitude (A and d are refinable parameters) (5–7). The following coherent scattering lengths were used: $b_{Li} = -0.190 \times 10^{-12}$ cm, $b_V = -0.038 \times 10^{-12}$ cm and $b_O = 0.580 \times 10^{-12}$ cm.

The high-resolution neutron powder diffraction pattern was fitted from the crystallographic description proposed by Shannon and Calvo in 1973 (1) from X-ray single-crystal diffraction. The room temperature structure of $LiVO_3$ was refined in the monoclinic space group $C2/c$ with $a = 10.1597_{(4)}$, $b = 8.4155_{(3)}$, $c = 5.8843_{(2)}$ Å, and $\beta = 110.505^\circ_{(2)}$. Preliminary cycles were performed to refine the

TABLE 1
High Resolution Neutron Powder Diffraction: Experimental Details

Data collection	
Radiation type	Neutron
Diffractometer	3T2, LLB–Saclay
Wavelength (Å)	1.2251
Sample container	Vanadium can
2θ Range (°)	5.0–125.7
2θ Step scan (°)	0.05
Monochromator	Ge (335)
Instrumental geometry	20 ^{3}He detectors
Crystal Data	
Chemical Formula	$LiVO_3$
Chemical Formula weight	105.88
T (K)	290
Cell setting	Monoclinic
Space group	$C2/c$
a (Å)	$10.1597_{(4)}$
b (Å)	$8.4155_{(3)}$
c (Å)	$5.8843_{(2)}$
β (°)	$110.505_{(2)}$
V (Å^3)	$471.23_{(1)}$
Z	8
Refinement	
Background	Polynome and Debye function
Excluded regions	5.0–13.0; 109.0–125.7
Full width at half maximum	Caglioti function
Profile shape function	Pseudo-Voigt
Structure refinement program	Fullprof (Rodriguez–Carvajal, 1990)
Weighting scheme	$w = 1/\sigma^2$; $\sigma^2 = y_i$
No. of reflections	759
No. of parameters refined	59
R_p	0.030
R_{wp}	0.036
R_{exp}	0.026
R_{Bragg}	0.049
R_F	0.031
χ^2	1.91

$R_p = \sum_i |y_i - y_{ci}| / \sum_i y_i$ $R_{wp} = \sqrt{\sum_i w_i (y_i - y_{ci})^2 / \sum_i w_i y_i^2}$ $R_{Bragg} = \sum_i |I_i - I_i^{calc}| / \sum_i I_i$ $R_F = \sum_i |\sqrt{I_i} - \sqrt{I_i^{calc}}| / \sum_i \sqrt{I_i}$

TABLE 2
Details of the Neutron Powder Thermodiffractometry Experiment (Given at 340 K)

Data collection	
Radiation type	Neutron
Diffractometer	D1B, ILL
Wavelength (Å)	2.525
Sample container	Vanadium can
2θ Range (°)	27.0–106.8
2θ Step scan (°)	0.2
Monochromator	Pyrolytic graphite (002)
Instrumental geometry	400 ^{3}He cells
Sample environment	Furnace
Temperature range	340–890 K
Crystal data	
Chemical Formula	$LiVO_3$
Chemical Formula weight	105.88
Cell setting	Monoclinic
Space group	$C2/c$
a (Å)	$10.1616_{(7)}$
b (Å)	$8.4281_{(7)}$
c (Å)	$5.8863_{(5)}$
β (°)	$110.466_{(6)}$
V (Å^3)	472.30
Z	8
Refinement	
Background	Polynomial function + Debye function
Excluded regions	27.0–29.0
Full width at half maximum	Caglioti function
Profile shape function	Gaussian
Structure refinement program	Fullprof running in sequential mode (Rodriguez–Carvajal, 1990)
Weighting scheme	$w = 1/\sigma^2$; $\sigma^2 = y_i$
No. of reflections	65
No. of parameters refined	21
R_p	0.034
R_{wp}	0.045
R_{exp}	0.019
χ^2	5.92

lattice constants, the atomic coordinates of the Li and O atoms and an overall atomic displacement parameter together with the profile parameters, the scale factor, and the parameters describing the background. Due to the small coherent scattering length of the vanadium nuclei, the V atomic coordinates were first fixed to the values obtained by Shannon and Calvo ($x = 0.2883$, $y = 0.0949$, and $z = 0.2669$) (1). When these coordinates were refined, the reliability factors remained stable and the resulting vanadium positions were very slightly changed. Finally, independent isotropic atomic displacement parameters were refined.

The treatment of the neutron powder thermodiffractometry data has been performed using a sequential mode available in the program Fullprof (3). In this procedure, the refined parameters resulting from the adjustment of one pattern are used as starting parameters for the next. It is an efficient and fast procedure to follow the thermal evolution of the various structural parameters.

3. ROOM TEMPERATURE STRUCTURE OF $LiVO_3$

3.1. Structural Refinement

Following the fitting procedure described in Section 2.3, correct reliability factors have been obtained, i.e., $R_{Bragg} = 0.073$, $R_F = 0.043$, and $\chi^2 = 3.10$. The resulting isotropic atomic displacement parameters being large for the lithium and oxygen atoms, anisotropic displacement parameters β_{ij} were refined (the displacements of the vanadium atoms remaining isotropic). The reliability factors were drastically improved since $R_{Bragg} = 0.049$, $R_F = 0.031$, and $\chi^2 = 1.91$. The parameters β_{ij} and equivalent atomic displacement parameters are given in Table 3 together with the fractional atomic coordinates. The structural results are in very good agreement with those previously proposed from X-ray single crystal diffraction (1). The fitting of the diffraction background using a Debye function provides a pair correlation distance d of about $2.86_{(2)}$ Å. Observed, calculated, and difference patterns are presented on Fig. 2 and Fig. 3 shows the crystal structure of $LiVO_3$ viewed down [010] (Fig. 3a) and [100] (Fig. 3b) directions. It clearly exhibits the alternating, along the b-axis, of bands of distorted LiO_6 octahedra and chains of VO_4 tetrahedra parallel to the c-axis.

Some attempts have been made to refine the structure of $LiVO_3$ in the noncentrosymmetric space group Cc which

TABLE 3
Fractional Coordinates, Atomic Displacement Parameters, and Anisotropic Displacement Parameters β_{ij} Resulting from the Rietveld Refinement

Atom	Site	x	y	z	B_{eq} (Å^2)	B_{iso} (Å^2)
Li(1)	4e	0	$0.9267_{(9)}$	$\frac{1}{4}$	2.15	—
Li(2)	4e	0	$0.2831_{(9)}$	$\frac{1}{4}$	2.32	—
V	8f	$0.287_{(3)}$	$0.084_{(3)}$	$0.265_{(5)}$	—	1.2
O(1)	8f	$0.1141_{(2)}$	$0.1112_{(2)}$	$0.1660_{(3)}$	1.10	—
O(2)	8f	$0.3563_{(3)}$	$0.2723_{(2)}$	$0.2819_{(3)}$	1.81	—
O(3)	8f	$0.3548_{(2)}$	$-0.0276_{(2)}$	$0.0762_{(3)}$	1.34	—

Atom	β_{11}	β_{22}	β_{33}	β_{12}	β_{13}	β_{23}
Li(1)	$0.008_{(1)}$	$0.006_{(1)}$	$0.022_{(3)}$	0	$0.095_{(1)}$	0
Li(2)	$0.008_{(1)}$	$0.004_{(1)}$	$0.030_{(3)}$	0	$0.009_{(2)}$	0
V	—	—	—	—	—	—
O(1)	$0.0037_{(2)}$	$0.0050_{(3)}$	$0.0062_{(5)}$	$-0.0006_{(2)}$	$0.0027_{(3)}$	$0.0005_{(3)}$
O(2)	$0.0080_{(3)}$	$0.0057_{(3)}$	$0.0118_{(6)}$	$-0.0034_{(2)}$	$0.0067_{(4)}$	$-0.0021_{(3)}$
O(3)	$0.0044_{(2)}$	$0.0077_{(3)}$	$0.0032_{(6)}$	$-0.0008_{(2)}$	$0.0023_{(3)}$	$-0.0016_{(3)}$

Note. Su's are given in parenthesis. The isotropic equivalent term B_{eq} is calculated from the trace of the diagonal B_i matrix: $B_{eq} = \frac{1}{3}\sum_i B_i$. For anisotropic atomic displacements, the exponent term takes the form $T(hkl) = \exp -(\beta_{11}h^2 + \beta_{22}k^2 + \beta_{33}l^2 + 2\beta_{12}hk + 2\beta_{13}hl + 2\beta_{23}kl)$.

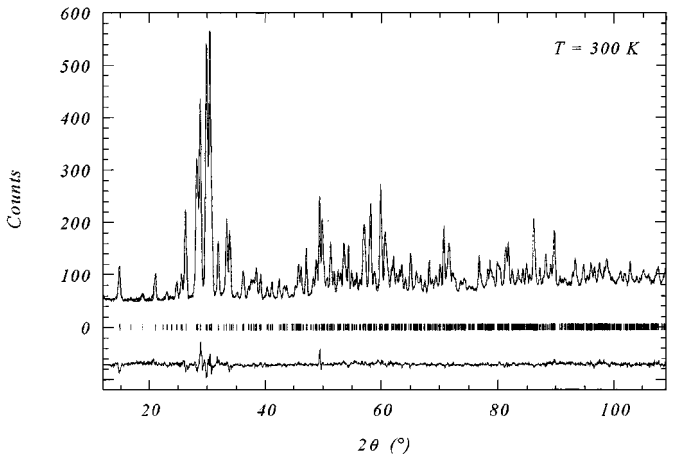

FIG. 2. Observed and calculated neutron powder diffraction patterns of $LiVO_3$ at room temperature. The lower field shows the difference $I_{obs} - I_{calc}$.

has the same extinction rules as the group $C2/c$. Thirty atomic coordinates (6 crystallographic sites for O, 2 for Li, and 2 for V) were then refined in the group Cc instead of 14 in the higher symmetry space group $C2/c$. The refinement of the coordinates and independent isotropic atomic displacement parameters led to slightly improved reliability factors, i.e., $R_{Bragg} = 0.066$ and $R_F = 0.040$ ($\chi^2 = 2.90$ instead of $\chi^2 = 3.10$). However, the refinement was unstable and the improvement is not really significant if one considers the large increasing of the number of parameters refined. Therefore, our neutron powder diffraction data are probably not accurate enough to unambiguously resolve the question regarding the choice of the $LiVO_3$ monoclinic space group.

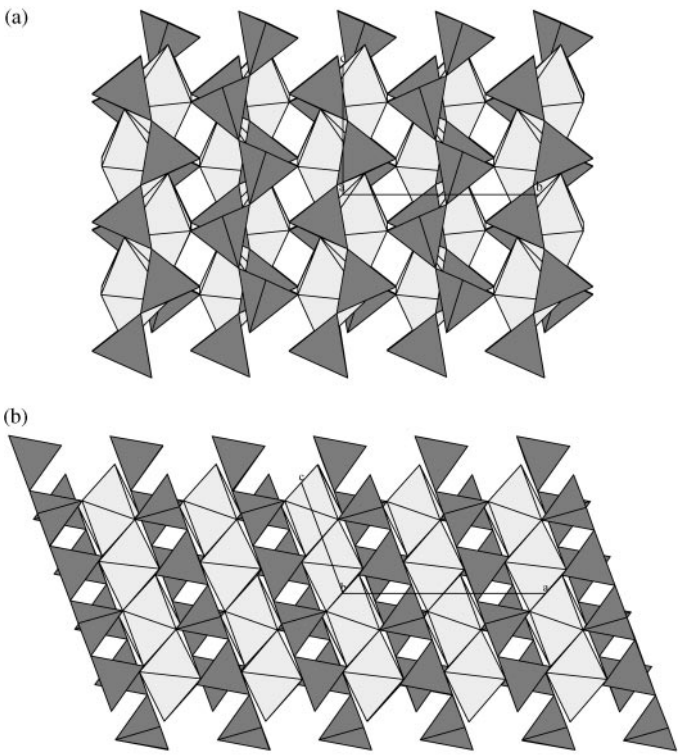

FIG. 3. Crystal structure of $LiVO_3$ viewed down [010] in (a) and [100] in (b) and showing the VO_4 tetrahedra (in gray) and LiO_6 octahedra (in white). For clarity, only the octahedra surrounding the Li(1) atoms are depicted.

3.2. Nuclear Density Maps

The refinement of the structure in the space group $C2/c$ being satisfactory, Fourier maps have been drawn using observed structure factors and calculated phases. These Fourier syntheses have been obtained using the program Gfourier based on a Fast Fourier Transform (FFT) subroutine (8). The Fourier maps, showing the nuclear densities, have been calculated in the (b, c) crystallographic plane for various layers along the a-axis.

Figure 4a shows the nuclear densities of the oxygen atoms in the (b, c) plane at $x = 0.138$. This map clearly exhibits the chains of the VO_4 tetrahedra running parallel to the c-axis, these tetrahedra being linked by the bridging oxygen atom O(3). The oxygen atoms O(2) and O(3) form a triangular face of the tetrahedra parallel to the (b, c) plane (shaded triangles on Fig. 4a and tetrahedra clearly seen on the 3D drawing presented on Fig. 3a). The chains of tetrahedra are separated by double bands of octahedra of the Li(1) and Li(2) atoms which are clearly evidenced on the Fourier map presented on Fig. 4b (Fourier synthesis in the (b, c) plane at $x = 0$). The octahedra of the Li(1) atoms form chains along the c-axis and are linked to the VO_4 tetrahedra by the oxygen atoms O(2). In the distorted octahedral environment of the Li(2) atoms, the largest oxygen–oxygen distance corresponds to the O(2)–O(2) distance. Therefore, all the polyhedra surrounding the Li^+ and V^{5+} cations share the O(2) oxygen atoms. This fact can explain the slightly elongated nuclear density along the c-axis observed on the O(2) oxygen sites (Fig. 4a). In conclusion, the VO_4 chains are separated by a double strip of edge-sharing oxygen octahedra of the Li(1) and Li(2) atoms.

3.3. Interatomic Distances and Displacement Ellipsoids

From the atomic coordinates, the interatomic Li–O distances have been calculated. The distances given in Table 4 show that the oxygen octahedra surrounding the Li(1) atoms are more regular than those of the Li(2) atoms which contain two very long bonds Li(2)–O(2) of 2.668 Å. This octahedral elongation along the c-axis leads to a greater average distance Li–O for the Li(2) shell than for the Li(1) one (2.286 Å against 2.148 Å). Ignoring the longer Li–O

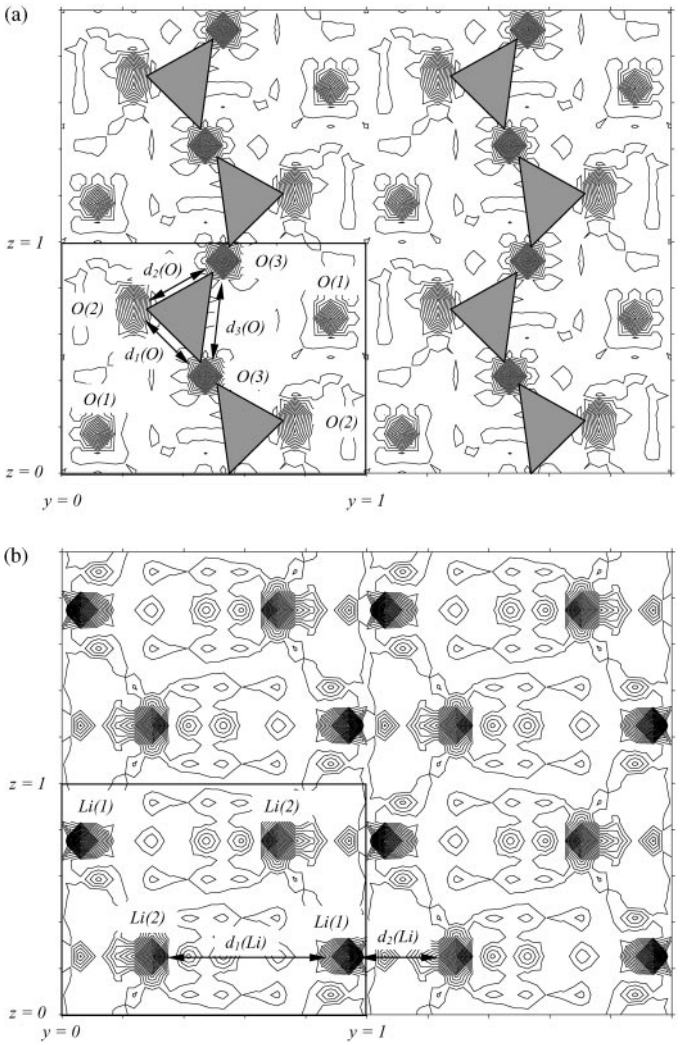

FIG. 4. Fourier maps in the (b, c) plane showing the nuclear densities of the oxygen atoms at $x = 0.138$ (a) and those of the lithium atoms at $x = 0$ (b). The shaded triangles represent the faces of the VO_4 tetrahedra parallel to the (b, c) plane. For clarity, the unit cell is doubled along the b and c axes.

distance, the Li(2) environment could be considered as a distorted tetrahedron.

The distances noted $d_1(O)$, $d_2(O)$, and $d_3(O)$ on the Fourier map presented on Fig. 4a have been calculated: $d_1(O) = 2.694$ Å, $d_2(O) = 2.797$ Å, and $d_3(O) = 2.979$ Å. The spread of the oxygen–oxygen distances clearly exhibits the large distortion of the triangular faces of the VO_4 tetrahedra parallel to the (b, c) plane.

The isotropic displacement parameters of the Li and O atoms being large, the anisotropic displacement parameters have been refined. The magnitude and the orientation of the resulting ellipsoids, associated with the probability density of lithium and oxygen atoms around their average site, have been found by solving the eigenvalue problem for the resulting 3×3 β_{ij}-matrix. Table 5 summarizes the root mean squared amplitudes of the Li and O nuclei displacements and the orientation of the ellipsoids with respect to the crystallographic axes.

TABLE 4
Li–O Interatomic Distances Given in Å

Bond	Distance
Li(1)–O(2)	2.012 × 2
Li(1)–O(1)	2.098 × 2
Li(1)–O(1)	2.335 × 2
⟨Li(1)–O⟩[a]	2.148
Li(2)–O(1)	2.021 × 2
Li(2)–O(3)	2.169 × 2
Li(2)–O(2)	2.668 × 2
⟨Li(2)–O⟩[a]	2.286

[a] Average distances.

As previously observed by Shannon and Calvo, the displacement ellipsoids of the Li atoms are strongly anisotropic since they are cylinder-shaped with a ratio of about 2 between the larger and the smaller amplitudes (1). Taking into account the orientation of the ellipsoids given in Table 5, it appears that the maximum amplitude is observed along the longest Li–O bond of the octahedra (Li(1)–O(1) and Li(2)–O(2) bonds). This suggests a possible disorder of the Li atoms around their average sites. On the other hand,

TABLE 5
Magnitude and Orientation of the Displacement Ellipsoids of the Li and O Atoms

Atom	RMS amplitudes (Å)	Angles (°) with $\vec{a}$	$\vec{b}$	$\vec{c}$
Li(1)	0.21	54.2	90.0	56.3
	0.15	90.0	0.0	90.0
	0.12	144.2	90.0	33.7
Li(2)	0.22	67.2	90.0	43.3
	0.15	22.8	90.0	133.3
	0.12	90.0	0.0	90.0
O(1)	0.14	53.7	142.4	94.2
	0.12	51.2	55.5	73.6
	0.08	59.6	76.9	163.1
O(2)	0.21	40.3	118.8	82.1
	0.12	96.6	139.3	124.2
	0.09	50.4	63.9	144.6
O(3)	0.17	75.0	161.0	84.7
	0.14	22.0	72.5	96.7
	0.06	74.4	97.1	171.5

Note. The root mean squared amplitudes have been calculated as follows: $RMS = \sqrt{B_i/8\pi^2}$.

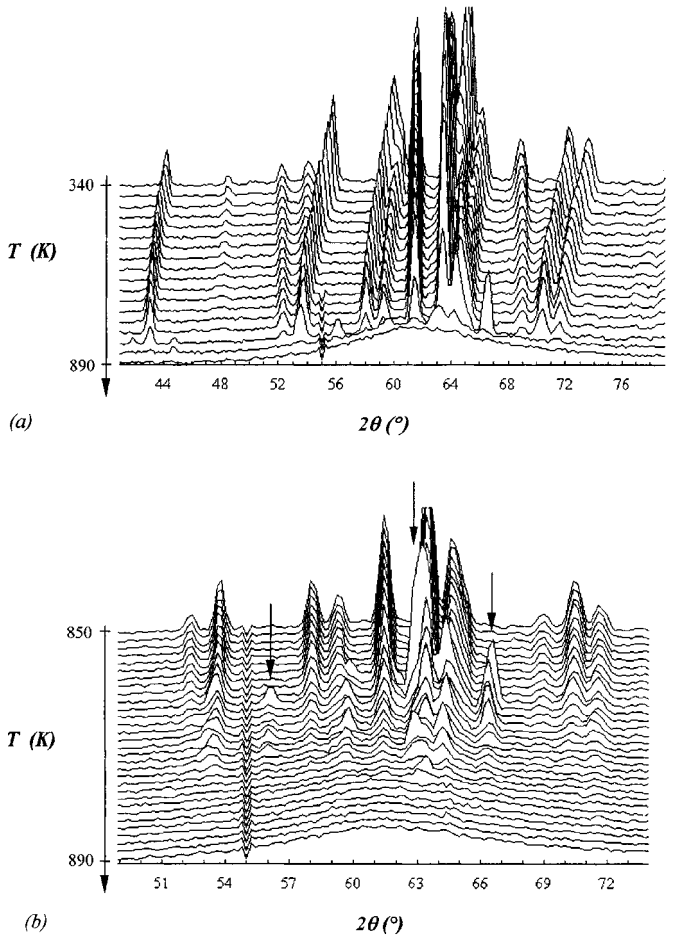

FIG. 5. Evolution of the neutron powder diffraction patterns, between 41 and 79° in 2θ, in the temperature range 340–890 K in (a). In order to clearly exhibit the solid-liquid transition, the same diffraction patterns have been plotted between 850 and 890 K in (b) in the angular range 49–74° in 2θ.

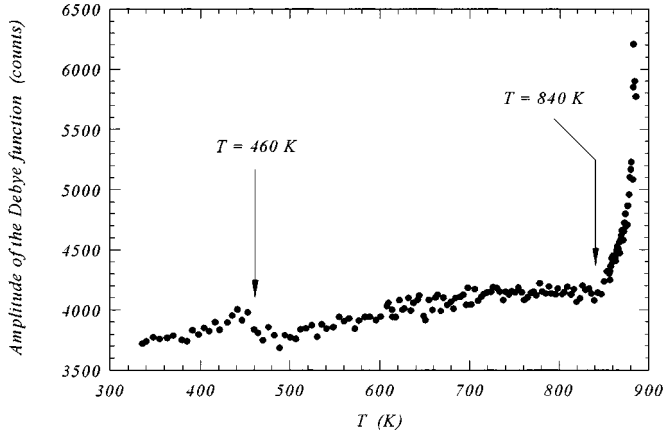

FIG. 6. Thermal evolution of the amplitude A of the Debye function used to describe the modulated diffraction background.

the same behavior is observed for the O(2) atoms, whereas the ellipsoids of the O(3) atoms are disc-shaped. Those of the O(1) atoms remain nearly isotropic, the equivalent atomic displacement parameter being smaller than those of the O(2) and O(3) oxygen atoms.

4. STRUCTURAL BEHAVIOR IN THE TEMPERATURE RANGE 340–890 K

The PSD available on the D1B instrument has been used to study *in situ* the structural evolution of the lithium metavanadate $LiVO_3$ in the temperature range 340–890 K. The melting temperature of $LiVO_3$ being about 880 K, the thermal behavior has been followed up to the solid-to-liquid transition (1).

The temperature dependent evolution of the neutron powder diffraction patterns (Fig. 5a) between the 340 and 890 K clearly shows the occurrence of one phase transition which corresponds to the solid–liquid phase transition. Some structural changes appear through the obvious angular shift of some Bragg reflections. The thermal expansion of the unit cell is suggested to be anisotropic since some reflections have no angular shifts.

The solid-to-liquid phase transition is clearly seen in Fig. 5b, which presents the evolution of the diffraction patterns between 850 and 890 K. The Bragg reflections vanish at about 878 K, whereas the diffraction background shows a concomitant increasing. Before the total disappearance of the solid phase, a metastable phase, whose the Bragg reflections are arrowed on Fig. 5b, grows and subsists over a temperature range of about 10 K. Above 878 K, the liquid phase is exhibited through the strong modulation of the diffraction background, the maximum being observed at 61.5° in 2θ.

Using the Debye function detailed in Section 2, the diffraction background has been adjusted over the whole temperature range. The first maximum of the modulation is associated with a pair correlation distance d of about 2.85 Å, which corresponds to a typical oxygen–oxygen distance. The thermal evolution of the amplitude A of this first modulation, refined for each pattern, is given on Fig. 6. Excluding the anomaly observed at 460 K, the amplitude shows a linear behavior from 340 to 840 K. Above 840 K, it exhibits a sharp increasing which can be attributed to the appearance of the liquid phase. The amplitude has a maximum at 890 K when only the liquid phase subsists. The lithium metavanadate being highly hygroscopic, the anomaly observed at 460 K can be associated with a dehydration of the sample. The hydrogen nuclei having a large incoherent scattering cross section, the dehydration of the powder is obviously accompanied by a decreasing of the background intensity.

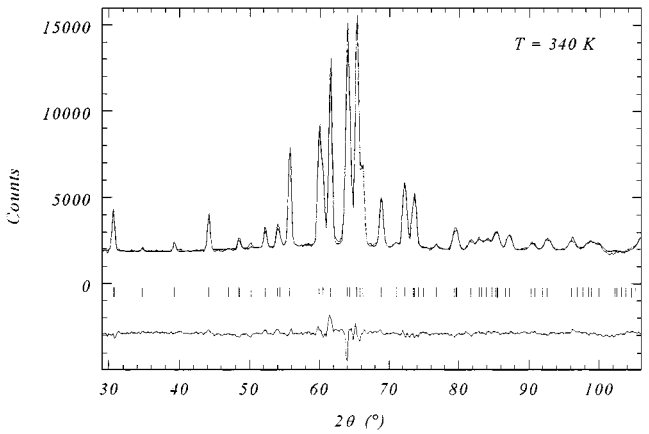

FIG. 7. Observed and calculated and difference neutron powder diffraction profiles at 340 K (data collected on the D1B instrument).

Starting from the crystallographic model fully described in Section 3, sequential refinements of a number of structural parameters have been performed in order to extract quantitative results from the neutron powder thermodiffractometry patterns. To avoid correlations, only few parameters were simultaneously fitted: the cell parameters, the Li and O coordinates, and two isotropic atomic displacement parameters B_{iso} [Li] and B_{iso} [O], taking into account, respectively, the displacements of the Li(1) and Li(2) atoms and those of the O(1), O(2), and O(3) atoms. Due to the small coherent scattering length of the vanadium nucleus and to the low resolution of the instrument D1B, the V coordinates were fixed. Figure 7 shows the observed, calculated, and difference patterns at 340 K.

Figure 8 presents the evolution of the reliability factor χ^2: from 340 to 460 K, χ^2 is of about 6.5 and then abruptly decreases to 4.8 above 460 K. This decreasing can be also attributed to the dehydration of the powdered sample. Between 840 and 880 K, the reliability factor χ^2 shows a spread characteristic of the appearance of the liquid phase. The growth of the metastable phase also contributes to the increasing of χ^2 in the temperature range 870–880 K. Finally, the solid phase vanishing is accompanied by a sharp increasing of the reliability factor.

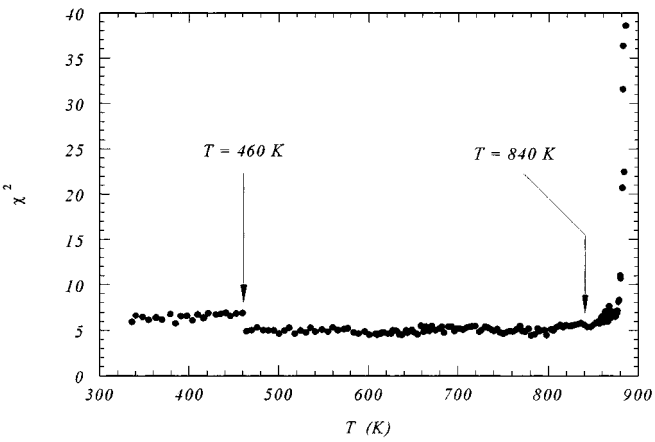

FIG. 8. Evolution of the reliability factor χ^2 as a function of the temperature. The decreasing observed at 460 K is associated with the dehydration of $LiVO_3$.

4.1. Anisotropic Thermal Expansion

From the sequential Rietveld refinements, the lattice expansion of $LiVO_3$ has been followed from 340 to 880 K. Figure 9 shows the thermal evolution of the parameters a, b, c, β, and V refined in the monoclinic space group $C2/c$. The monoclinic angle β and the lattice constant b show large variations over the whole temperature range: β decreases from 110.5° to 109.9° and b linearly increases from 8.43 to 8.75 Å. On the contrary, the other cell parameters show very weak thermal expansion, especially for c, which exhibits a variation of about 0.005 Å. Nevertheless, the nonlinear thermal behavior of the parameter a below 690 K should be noted.

The relative thermal expansions have been calculated between 460 and 880 K. Figure 10 shows the temperature-dependent evolutions of $\Delta a/a$, $\Delta b/b$, $\Delta c/c$, and $\Delta V/V$. From their thermal behavior, the relative lattice expansion coefficients have been deduced. The following values have been determined:

$$\alpha_a = 4.8 \times 10^{-6}\ K^{-1};\ \alpha_b = 76.9 \times 10^{-6}\ K^{-1};$$

$$\alpha_c = 0.6 \times 10^{-6}\ K^{-1};\ \alpha_V = 88.6 \times 10^{-6}\ K^{-1}.$$

These coefficients clearly exhibit the strongly anisotropic character of the lattice expansion which is manifestly larger perpendicularly to the VO_4 tetrahedra chains.

4.2. Structural Disorder

From the atomic coordinates of the Li and O atoms, interatomic distances have been deduced. From the y coordinates of the Li(1) and Li(2) atoms, the distances noted d_1(Li) and d_2(Li) on the Fourier map presented on Fig. 4b, have been calculated and their thermal evolutions are given on Fig. 11. From 340 up to 690 K, the two Li–Li distances show a linear thermal behavior, but, above 690 K, the distances tend to be closer. Just below the solid–liquid phase transition, the distances d_1(Li) and d_2(Li) are respectively equal to 4.9 and 3.9 Å. Therefore, it seems that a quasi-liquid disorder appears in the (b, c) crystallographic plane containing the Li^+ cations.

Considering that the O(2) and O(3) oxygen atoms are almost in the same (b, c) plane at $x \approx 0.138$, the oxygen–oxygen distances in this plane have been calculated. Three

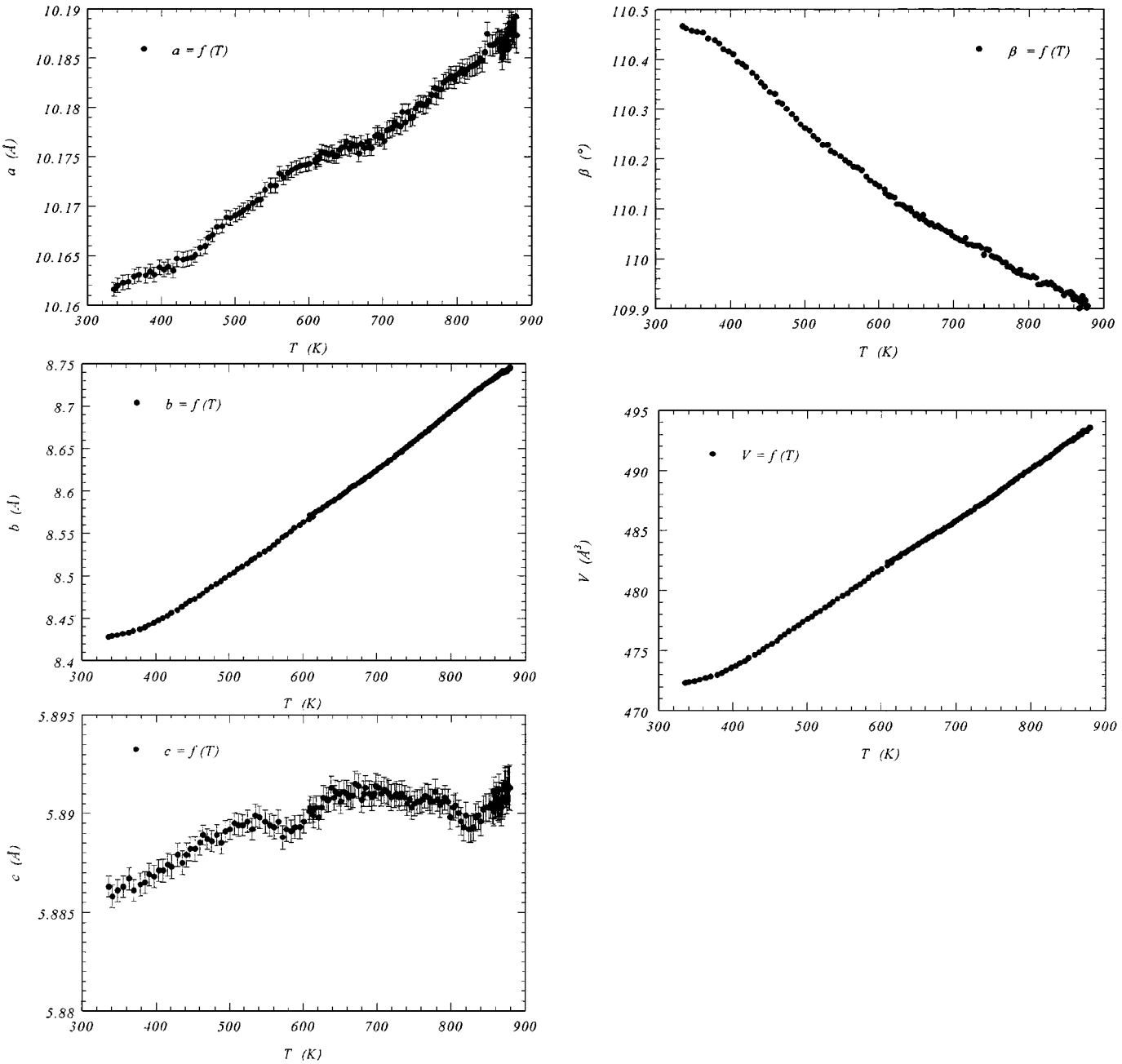

FIG. 9. Temperature-dependent evolution of the cell parameters a, b, c, β, and V given in the monoclinic space group $C2/c$.

couples of distances have been determined: d_1(O), d_2(O), and d_3(O) plotted on the Fourier map presented on Fig. 4a. Their evolutions are given on Fig. 12. It clearly appears that the thermal variations of the O(2)–O(3) distances are larger than those of the O(3)–O(3) ones (the distance d_3(O) remains nearly constant). This peculiar behavior is not really surprising since all the polyhedra surrounding the Li^+ and V^{5+} cations share the O(2) oxygen atoms. Therefore, it seems that the VO_4 tetrahedra undergo a shear in a direction parallel to the c-axis and the thermal evolution of the O–O distances indicates that the tetrahedra distortion is enlarged when the temperature increases.

Finally, the isotropic atomic displacement parameters of the Li and O atoms (noted B_{iso} [Li] and B_{iso} [O]) were followed as a function of the temperature. Their thermal evolution is depicted on Fig. 13. In agreement with the high-resolution neutron powder diffraction study presented in Section 3, the Li atoms have larger atomic displacement parameters than the O atoms. The larger disorder around the Li crystallographic sites is probably related to the

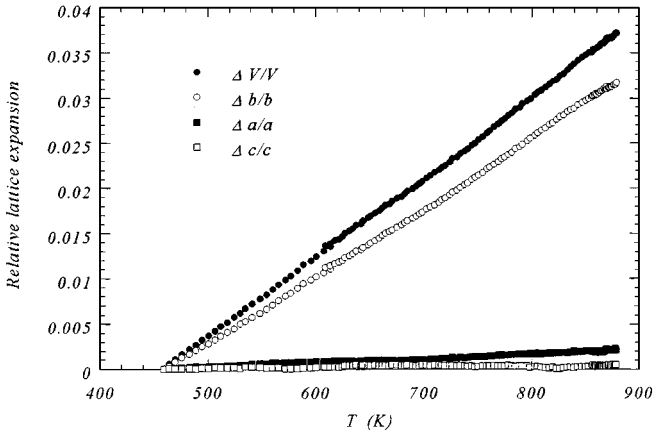

FIG. 10. Evolution of the $\Delta a/a$, $\Delta b/b$, $\Delta c/c$, and $\Delta V/V$ relative thermal expansions.

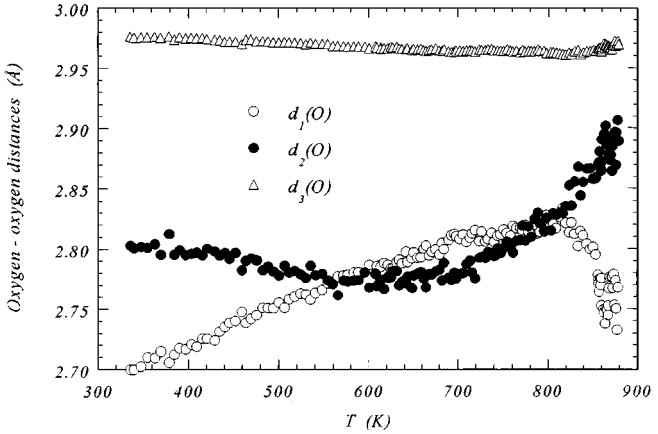

FIG. 12. Thermal evolution of the O–O distances in the (b, c) crystallographic plane at $x \approx 0.138$. The distances noted d_1(O), d_2(O), and d_3(O) are those plotted on the Fourier map presented on Fig. 3.

existence of diffusive motions of the Li^+ cations in $LiVO_3$. It has to be noticed that the oxygen displacement parameter B_{iso} [O] shows a linear behavior up to 840 K, whereas the lithium displacement parameter B_{iso} [Li] linearly increases up to 690 K and then seems to be stable up to 840 K. Therefore, above 840 K, the drastic increasing of the atomic displacement parameters can be correlated to the change of the interatomic distances, the two phenomena contributing to the enhancement of the structural disorder especially on the Li sites.

5. DISCUSSION

5.1. Space Group of the Room Temperature Structure of $LiVO_3$

From the measurements of pyroelectric current, several authors have stated that lithium metavanadate $LiVO_3$ undergoes a ferroelectric-to-paraelectric phase transition at 678 K approximately (9–11). The appearance of this transition is obviously conditioned by the existence of a noncentrosymmetric structure in the ferroelectric phase. Therefore, the refinement of the room temperature structure in the centrosymmetric space group $C2/c$ is not in agreement with the polar nature of this phase. A similar problem has been already encountered in the isomorphic $NaVO_3$ compound since its crystallographic structure was initially refined in the space group $C2/c$ by Marumo *et al.* in 1974 (12). In 1975, Ramani *et al.* have deduced that its room temperature structure could be refined in both space groups Cc and $C2/c$ (13). They stated that the transition observed at about 650 K in $NaVO_3$ could be attributed to a ferroelectric-to-paraelectric phase transition from the structure with space group Cc to a clinopyroxene structure with space

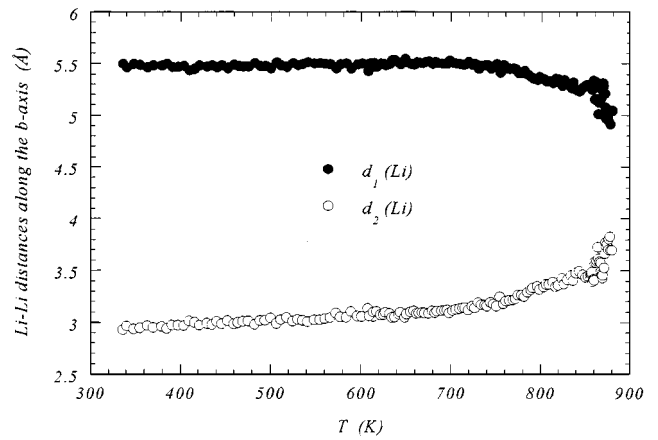

FIG. 11. Thermal evolution of the Li–Li distances in the (b, c) crystallographic plane at $x = 0$. The distances noted d_1(Li) and d_2(Li) are those plotted on the Fourier map presented on Fig. 4.

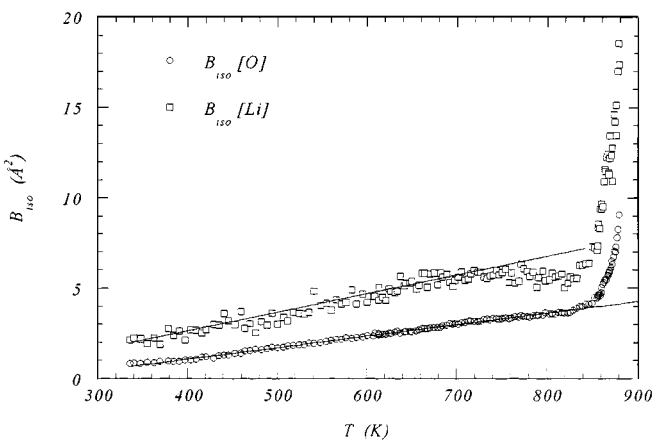

FIG. 13. Temperature dependent evolution of the isotropic atomic displacement parameters associated with the Li and O atoms.

group $C2/c$. They assigned this transition to the reorientation of the displacement ellipsoids of the atoms rather than to a major change in the structure. This hypothesis was confirmed later by Shaikh *et al.* (14, 15). In the case of the compound $LiVO_3$, it is possible that such a similar phenomenon occurs. From our high-resolution neutron powder diffraction data, some attempts have been done to refine the structure in space group Cc rather than in space group $C2/c$. A slight decreasing of the reliability factors has been observed but, taking into account the larger number of parameters refined, this improvement cannot be really considered as satisfactory. In conclusion, the structural changes between the space groups Cc and $C2/c$ are probably too small to unambiguously solve the symmetry problem from our neutron powder diffraction data. However, it has to be mentioned that even though the structure is of poor quality, the structure of $LiVO_3$ has been solved in the noncentrosymmetric space group Cc by Mahe and Lee in 1973 (16).

However, the ferroelectric-to-paraelectric surely exists in $LiVO_3$. Indeed, the Arrhenius plot of the electrical conductivity presented on Fig. 1 does not respect a linear behavior over the whole temperature range. Above 690 K, a drastic change in the slope is observed, this anomaly being related to an increasing of the activation energy. In agreement with the pyroelectric current measurements (9–11), this slope change might be associated with the ferroelectric-to-paraelectric phase transition. From the neutron powder thermodiffractometry experiment, this phase transition is not clearly evidenced since the reliability factor χ^2 presents no anomaly around 690 K. However, the cell parameter a does not exhibit a typical linear behavior below 690 K and the displacement parameter of the Li(1) and Li(2) atoms show an unusual evolution above 690 K. Indeed, the parameter B_{iso} [Li], which linearly increases up to 690 K, seems to be nearly constant between 690 and 840 K. On the other hand, the Li–Li distances in the (b, c) plane, noted d_1(Li) and d_2(Li), tend to be closer above 690 K. Therefore, even if no evident sign of the phase transition has been evidenced, a peculiar behavior is observed on the lithium crystallographic sites. In reference to the problem encountered in $NaVO_3$, it could be proposed that the ferroelectric-to-paraelectric phase transition consists of reorientations of the anisotropic displacement ellipsoids of the lithium atoms.

5.2. Structural Disorder and Lithium Mobility

The high resolution neutron powder diffraction study has shown that the structure could be described as an alternating, along the b-axis, of distorted VO_4 tetrahedra chains running parallel to the c-axis and a double strip of LiO_6 octahedra which are also parallel to the c-axis. The octahedra surrounding the Li(2) atoms have been shown to be more distorted than those surrounding the Li(1) atoms. The refinement of the anisotropic displacement parameters of the lithium atoms has exhibited a strong anisotropy of the displacement ellipsoids on the two Li(1) and Li(2) sites. Indeed, the ellipsoids are cylinder-shaped with a ratio of about 2 between the larger and the smaller amplitudes. Moreover, the direction of the maximum amplitude nearly coincides with the longest Li–O bond which is parallel to the c-axis. This peculiar behavior, observed on both sites, suggest a positional disorder of the Li^+ cations along the c-axis. Such a disorder was already proposed from high-temperature Raman spectroscopy studies by Grzechnik *et al.* (17). The band observed at 185 cm^{-1} was assigned to the Li–O motions increasing with the temperature, suggesting an enhancement of the thermal disorder especially on the Li(2) site. All these elements allow us to suggest that the Li^+ cations mobility is certainly at the origin of the high ionic conductivity measured in $LiVO_3$.

As shown on the Fourier map presented on Fig. 4b, at room temperature, the shortest Li–Li distance imposes diffusion paths parallel to the c-axis. These preferential paths are consistent with the elongated displacement ellipsoids around the Li sites, especially on the Li(2) one. The diffusive motions of the Li^+ cations along the c-axis probably involve distortions of the oxygen tetrahedra and octahedra. As shown by neutron powder thermodiffractometry, when the distances d_1(Li) and d_2(Li) tend to be equal, the oxygen–oxygen distances in the VO_4 tetrahedra are strongly modified. Furthermore, a modulated background is observed on the neutron diffraction patterns from 340 K. The first maximum of the modulation is associated with a pair correlation distance of 2.85 Å which is very close to the average oxygen–oxygen distance in the VO_4 tetrahedra ($\approx$2.82 Å at room temperature). Therefore, the existence of this modulation can be certainly correlated to the strong distortion of the VO_4 tetrahedra due to the diffusive motions of the Li^+ cations. Finally, the thermal evolution of the distances d_1(O) and d_2(O) has shown that the VO_4 tetrahedra probably undergo a shear in a direction close to the c-axis. The chemical bonds are anisotropically distributed and the force constants are weaker along the b-axis. This phenomenon could explain the strong anisotropic character of the lattice expansion along the b-axis.

In conclusion, the tendency of the VO_4 tetrahedra to rotate or to be distorted implies that the oxygen atomic motions are strongly correlated. This phenomenon is evidenced through a short-range order characterized by a pair correlation distance of about 2.85 Å and anisotropic displacement ellipsoids of the oxygen atoms, especially on the O(2) and O(3) oxygen sites.

5.3. Solid-to-Liquid Phase Transition

Neutron powder thermodiffractometry experiments have been performed in order to study the thermal behavior of the lithium metavanadate over the temperature range

340– 890 K. The melting temperature of $LiVO_3$ being of about 880 K, all the structural parameters have been followed up to the solid–liquid transition. From the thermal evolution of the Li–Li distances and the nuclear density maps, it is possible to suggest that, at low temperature, the diffusion of Li^+ ions essentially occurs along the *c*-axis. Above 840 K, the rapid increasing of the modulated background is associated with an increasing disorder linked to the appearance of the liquid phase. The short-range order of the solid phase is progressively replaced by the larger disorder in the liquid phase. When the solid and liquid phases coexist, the increasing of the displacement parameters of the Li atoms and the modification of the distances d_1(Li) and d_2(Li) along the *b*-axis suggest that a quasi-liquid disorder on the Li sites appears in the (*b*, *c*) plane. This quasi-liquid disorder can explain the enhanced conductivity.

6. CONCLUSIONS

A structural investigation of the thermal behavior of the lithium metavanadate $LiVO_3$ has been performed from temperature-dependent neutron powder diffraction experiments. The following results have been found:

(i) The monoclinic cell presents a strongly anisotropic lattice expansion over the whole temperature range. The relative lattice expansion coefficient along the *b*-axis is approximately 100 times larger than the one determined along the *c*-axis.

(ii) An important structural disorder has been observed on the lithium crystallographic sites. From high-resolution neutron powder diffraction, cylinder-shaped ellipsoids with a ratio of about 2 between the larger and the smaller amplitudes have been exhibited. These anisotropic displacement ellipsoids are certainly related to a positional disorder of the Li atoms along the *c*-axis. This result suggests that the Li^+ cations are certainly at the origin of the high ionic conductivity observed in $LiVO_3$.

(iii) The diffusive motions of the Li^+ cations involve strong distortions of the VO_4 tetrahedra which are clearly evidenced through the short-range order characterized by a pair correlation distance of about 2.85 Å and anisotropic displacement ellipsoids on the O(2) and O(3) oxygen sites.

(iv) The ferroelectric-to-paraelectric phase transition is not clearly seen from the thermal evolution of the structural parameters. This suggests that the phase transition is probably associated with very slight structural changes such as reorientations of the displacement ellipsoids of the lithium atoms.

REFERENCES

1. R. D. Shannon and C. Calvo, *Can. J. Chem.* **51,** 265 (1973).
2. J.-C. Valmalette, S. Villain, C. Leroux, and J.-R. Gavarri, "Proceeding of the 5th International Conference on Nanostructured Materials," Sendaï, August 20–25, 2000.
3. J. Rodriguez-Carvajal, "Fullprof. A program for Rietveld Refinement and Pattern Matching Analysis," Abstracts of the Satellite Meeting on Powder Diffraction of the XVth Congress of the International Union of Crystallography, 127, 1990.
4. G. Caglioti, A. Paoletti, and F. P. Ricci, *Nucl. Instrum.* **3,** 223 (1958).
5. B. T. M. Willis, "Chemical Applications of Thermal Neutron Scattering." Oxford Univ. Press, Oxford, 1973.
6. P. Aldebert, A. J. Dianoux, and J. P. Traverse, *J. Phys.* **40,** 1005 (1979).
7. Ch. Muller, M. Anne, and M. Bacmann, *Solid State Ionics* **111,** 27 (1998).
8. J. Gonzalez-Platas and J. Rodriguez-Carvajal, "Graphic Fourier Program." 2000. *http://www-llb.cea.fr/fullweb/others/newfour.htm.*
9. T. A. Patil, V. M. Jamadar, and S. H. Chavan, *Indian J. Phys. A* **62,** 341 (1988).
10. A. P. Kashid, V. V. Patil, and S. H. Chavan, *Bull. Mater. Sci.* **12,** 57 (1989).
11. S. H. Chavan and A. P. Kashid, *Ferroelectrics* **102,** 199 (1990).
12. F. Marumo, M. Isobe, S. Iwai, and Y. Kondo, *Acta Crystallogr. B* **30,** 1628 (1974).
13. K. Ramani, A. M. Shaikh, B. S. Reddy, and M. A. Visvamitra, *Ferroelectrics* **9,** 49 (1975).
14. A. M. Shaikh, M. A. Viswamitra, and P. S. Narayanan, *Ferroelectrics* **20,** 311 (1978).
15. A. M. Shaikh, *Ferroelectrics* **107,** 219 (1990).
16. Mahe and Lee, *C. R. Hebd. Séances Acad. Sci. C* **277,** 307 (1973).
17. A. Grzechnik and P. F. McMillan, *J. Phys. Chem. Solids* **56**(2), 159 (1995).